Cite as:
Capponi, L., Zaletelj, K., Slavič, J. (2025).
Thermoelasticity-based stress mode-shape identification in rotating structures.
Mechanical Systems and Signal Processing, 240, 113370.
https://doi.org/10.1016/j.ymssp.2025.113370

Thermoelasticity-based stress mode-shape identification in rotating structures

Lorenzo Capponi*, Klemen Zaletelj, Janko Slavič*

Faculty of Mechanical Engineering, University of Ljubljana, Aškerčeva cesta 6, Ljubljana, 1000, Slovenia,

Abstract

In experimental modal analysis of rotating structures, optical methods provide full-field and non-contact alternatives to traditional sensors. Thermoelastic stress analysis was recently related to experimental modal analysis and shown to offer a non-contact, full-field approach for stress mode shape measurement by capturing minute (typically below 1 mK) surface temperature fluctuations associated with dynamic loading. However, applying thermoelasticity to large-scale moving structures remains challenging due to motion artifacts and the need for reliable tracking of surface points to preserve spatial alignment across frames. This study introduces infrared ArUco markers to track the rigid in-plane motion of a rotating aluminum beam undergoing out-of-plane vibration during thermoelastic measurements. Frame-to-frame transformations are applied to de-rotate the thermal video, enabling accurate modal parameters and full-field mode shapes identification. An uncertainty analysis is performed to assess the impact of motion compensation, revealing sub-pixel transformation errors across diverse experimental scenarios. By extending thermoelasticity-based stress modal shape measurements to rotating structures, the introduced method enables a non-contact stress measurements in dynamic environments, opening new opportunities for structural health monitoring and fatigue assessment of rotating components.

Keywords: Rotating Structures; Thermoelasticity; Computer-Vision; Structural Dynamics; Health Monitoring.

---

*Corresponding authors: lorenzo.capponi@fs.uni-lj.si, janko.slavic@fs.uni-lj.si

1. Introduction

Rotating components are integral to many engineering systems, where structural vibrations can critically impact their reliability, durability, and overall performance [1, 2]. To mitigate and control these effects, the accurate identification of modal parameters, such as natural frequencies, mode shapes, and damping, is essential for fatigue assessment, design optimization, and structural health monitoring (SHM) [3, 4]. However, conducting experimental modal analysis (EMA) on rotating structures presents significant challenges [5]. Traditional contact sensors, as accelerometers or strain gauges, can alter the dynamic response due to mass-loading effects and are often difficult to deploy in harsh environments or on complex geometries due to wiring constraints and data-transmission issues [6, 7]. These constraints have accelerated the employment of optical, non-contact techniques [8], which are particularly well-suited for the dynamic characterization of rotating components [9, 10], while also enabling full-field information and high-resolution data acquisition [11–14].

For rotating structures, commonly adopted methods for structural health monitoring include Digital Image Correlation (DIC) [15, 16], Laser Doppler Vibrometry (LDV) [17, 18], and Shearography [19], which is particularly sensitive to out-of-plane surface displacement gradients. While Infrared Thermography (IRT) has been widely explored for surface temperature mapping and defect detection in rotating machinery components [20, 21], its application is typically limited to static thermal fields [22, 23]. In contrast, Thermoelastic Stress Analysis (TSA) extends the use of infrared detection to dynamic scenarios by capturing transient thermal responses induced by cyclic mechanical loading [24]. Based on the thermoelastic effect, first observed by Weber [25] in 1830 and theoretically explained by Thomson (later Lord Kelvin) in 1853 [26], which links reversible surface temperature variations to stress fluctuations [27], TSA enables full-field, non-contact insight into structural behavior under dynamic excitation [28]. Recent advancements in infrared detector technology, including enhanced spatial resolution, increased sampling rates, and reduced noise levels (on the order of tens of milliKelvin), have significantly improved the feasibility of TSA for structural dynamics and fatigue assessment [29]. In fact, in recent years, several studies have demonstrated the viability of TSA for EMA and SHM [30, 31]. In 2020, Capponi et al. [32] introduced a modal decomposition framework for full-field fatigue damage characterization. In 2021, Molina-Viedma et al. [33]

explored TSA for identifying high-frequency mode shapes and later extended the approach to multi-harmonic excitations using a periodogram-based spectral analysis [34]. In 2023, Zaletelj et al. [35] proposed a strain-based EMA method relying on TSA-derived data, while, in 2025, Šonc et al. [36] developed a multiaxial fatigue criterion using full-field TSA-based stress measurements.

Despite these promising developments, the application of TSA to rotating structures remains challenging [29]. For small-scale displacements, the edge effects, manifesting as apparent stress concentrations near structural boundaries, are typically mitigated using motion compensation strategies such as combining TSA with DIC [37, 38], optical flow-based correction [39], or blob-detection tracking in the infrared domain [40]. However, the adaptation of motion compensation strategies to accommodate larger-scale rotational motion remains a significant open problem for TSA-based EMA, where robust frame-to-frame alignment is essential to reconstruct full-field, time-resolved stress histories.

This study addresses the current lack of effective methods for applying TSA to structures undergoing in-plane rotation, where rigid body motion interferes with accurate stress field reconstruction. By combining thermoelasticity with computer-vision techniques, the proposed method enables full-field identification of out-of-plane structural dynamics (i.e., mode shapes) in rotating structures. Specifically, infrared ArUco markers are employed to track frame-to-frame transformations and revert the in-plane rigid motion of a rotating aluminum beam subjected to random vibration. ArUco markers are selected for their robustness to perspective distortions and partial occlusions, as well as their binary grid-based unique IDs, which reduce reliance on complex feature matching [41, 42]. Such properties make ArUco well-suited for tracking both small and large displacements in dynamic scenarios [43–45]. An uncertainty analysis is also performed to quantify the accuracy of the motion compensation across different experimental conditions.

This manuscript is organized as follows. The theoretical background of thermoelasticity, structural dynamics, and image processing is given in Sec. 2. The proposed method for thermoelasticity-based identification of mode shapes in rotating structures is presented in Sec. 3. Sec. 4 describes experimental setup and infrared measurement and processing, while in Sec. 5 the results from the experimental campaign are presented and discussed. Sec. 6 draws the conclusions.

2. Theoretical background

2.1. Thermoelasticity

Thermoelasticity is a non-contact, high-sensitivity technique for full-field stress measurement based on the reversible conversion between mechanical and thermal energy when materials are subjected to external load-induced volume changes [25, 26]. This phenomenon, known as the thermoelastic effect, is inherently linked to the elastic and thermodynamic behavior of materials and has been long recognized and incorporated into structural theories [28]. For stresses within the elastic limit, the energy conversion is nearly reversible (i.e., isentropic), and surface temperature variations are directly related to the first invariant of the Cauchy stress tensor, which corresponds to the sum of the normal stresses [29]. By coupling thermodynamic principles with continuum mechanics, the fundamental thermoelastic relation for isotropic, plane-stress conditions can be written as [46, 47]:

$$\Delta\sigma_{xx} + \Delta\sigma_{yy} = -\frac{\rho\, C_\sigma}{\alpha}\frac{\Delta T}{T_0}, \tag{1}$$

where $\Delta\sigma_{xx}$ and $\Delta\sigma_{yy}$ are the variations of the in-plane normal stresses, ρ is the material density, C_σ is the specific heat at constant stress, α is the coefficient of linear thermal expansion, ΔT is the surface temperature change, and T_0 is the reference temperature.

Material properties can be grouped into the thermoelastic coefficient K_m, which characterizes the sensitivity of temperature variations to stress changes [48]. K_m can be determined from literature data, experimental calibration using strain gauges and Lamé theory, or numerical calculations [48]. The theoretical expression of K_m is [29]:

$$K_m = -\frac{\alpha\, T_0}{\rho\, C_\sigma}. \tag{2}$$

Under dynamic loading, cyclic stresses produce adiabatic temperature oscillations proportional to the stress amplitude [49]. High-performance infrared detectors, combined with phase-sensitive data processing techniques, enable the detection of these small temperature changes (typically in the milliKelvin range) [50, 51].

By measuring the surface temperature variation $\Delta T_{i,j}(t)$ at each pixel location (i, j) of a structure undergoing dynamic loading, the corresponding full-field stress variation $\Delta\sigma_{i,j}(t)$ can be approximated under a dominant uniaxial stress assumption as:

$$\Delta\sigma_{i,j}(t) = \frac{\Delta T_{i,j}(t)}{K_m}. \tag{3}$$

This uniaxial assumption provides a useful approximation in simple cases. For more complex structures exhibiting multiaxial stress states, the first invariant approach remains theoretically valid; however, a comprehensive multi-component stress analysis would be necessary for accurate quantification.

2.2. Mode Shapes Identification

A spatial model describing the forced response of a multiple-degree-of-freedom (MDOF) mechanical system is governed by the following equilibrium equation [52]:

$$\mathbf{M}\ddot{\mathbf{x}}(t) + \mathbf{C}\dot{\mathbf{x}}(t) + \mathbf{K}\mathbf{x}(t) = \mathbf{f}(t), \tag{4}$$

where $\mathbf{f}(t)$ represents the vector of applied excitation forces, and $\mathbf{M}, \mathbf{C}, \mathbf{K}$ are the mass, damping, and stiffness matrices, respectively. Transforming Eq. (4) into the frequency domain under the assumption of harmonic excitation leads to the structural response model [53]:

$$\mathbf{X}(\omega) = \mathbf{H}(\omega)\mathbf{F}(\omega), \tag{5}$$

where $\mathbf{H}(\omega)$ is the complex receptance frequency response function (FRF) matrix. The FRFs carry information on the system's natural frequencies, mode shapes, and damping characteristics, enabling the identification of modal parameters [52]. In experimental measurements, the FRF can be estimated using the H_1 estimator, which is defined as [52]:

$$H_1(\omega) = \frac{G_{XF}(\omega)}{G_{FF}(\omega)}, \tag{6}$$

where $G_{XF}(\omega)$ is the cross-power spectral density between the response $X(\omega)$ and the force $F(\omega)$, and $G_{FF}(\omega)$ is the auto-power spectral density of the force. To extract modal parameters, the Least-Squares Complex Frequency (LSCF) method is employed to identify system poles, which correspond to the natural frequencies and damping from the estimated FRF [54]. The identified poles are subsequently used with the Least-Squares Frequency Domain

(LSFD) algorithm to extract the modal constants $\mathbf{A}^x$ [55]. Assuming excitation at a single location (z), the mode shapes can be estimated from the modal constants as:

$$\phi_n^x = \frac{A_n^x}{\phi_z}, \tag{7}$$

where A_n^x is the modal constant at the n-th location, and ϕ_z is the mode shape value at the excitation point z.

2.3. Geometric transformations identification

The relationship between corresponding points $\mathbf{P}$ and $\mathbf{P}'$ in a pair of images undergoing a planar geometric transformation can be represented in homogeneous coordinates ($\mathbb{R}^3$) as [56]:

$$\mathbf{P}' = \mathbf{Q}\,\mathbf{P}, \tag{8}$$

where $\mathbf{Q} \in \mathbb{R}^{3\times3}$ is the transformation matrix that maps points from the original image plane to the transformed image plane. This planar transformation assumes that the points lie on a common plane and that the camera's optical axis is perpendicular to this plane, with primarily rotational motion and minimal perspective distortion. Under these conditions, the mapping is valid as a 2D projective transformation. For scenes with significant depth variation or translation, more general models such as full projective geometry or structure-from-motion are required [56]. The transformation matrix $\mathbf{Q}$ is defined as [56]:

$$\mathbf{Q} = \begin{bmatrix} q_{11} & q_{12} & q_{13} \\ q_{21} & q_{22} & q_{23} \\ q_{31} & q_{32} & q_{33} \end{bmatrix}, \tag{9}$$

and its structure determines the nature of the transformation. A general homography captures rotation, translation, scaling, shearing, and perspective distortion [56]. However, when perspective effects are negligible, the transformation simplifies to an affine form, in which the last row of $\mathbf{Q}$ becomes $(0, 0, 1)$. If, additionally, the transformation preserves distances and angles, it further reduces to a Euclidean transformation, consisting solely of rotation and translation. In this case, $\mathbf{Q}$ takes the following form [57]:

$$\mathbf{Q} = \begin{bmatrix} \cos\theta & -\sin\theta & r_i \\ \sin\theta & \cos\theta & r_j \\ 0 & 0 & 1 \end{bmatrix}. \tag{10}$$

Here, θ is the rotation angle, measured counterclockwise from the positive i-axis, and r_i and r_j are the translation components along the i- and j-axes, respectively. Inverting Eq. (8) provides a means to restore transformed points to their original reference frame by reversing the rigid motion effects, resulting in:

$$\hat{\mathbf{P}} = \mathbf{Q}^{-1}\mathbf{P}'. \tag{11}$$

Hat symbol in $\hat{\mathbf{P}}$ describes back-projected coordinates of a transformed point into reference frame. Expanding Eq. (11) for a Euclidean transformation leads to the element-wise inverse transformation:

$$\begin{cases} \hat{i} = \cos\theta \cdot (i' - r_i) + \sin\theta \cdot (j' - r_j), \\ \hat{j} = -\sin\theta \cdot (i' - r_i) + \cos\theta \cdot (j' - r_j). \end{cases} \tag{12}$$

3. Thermoelasticity-based identification of mode shapes in rotating structures

In this section, the methodology developed to identify mode shapes of rotating structures based on thermoelastic measurements is presented. The approach consists of detecting ArUco markers in images acquired by an infrared camera and using them to estimate in-plane rigid rotation matrices. These matrices are then inverted to compensate for the motion and realign the video frames to a fixed spatial reference. This correction enables the extraction of accurate and consistent temperature-based time histories. After motion compensation, the thermoelasticity principle is used to derive full-field stress information on the de-rotated structure, and frequency-domain techniques are applied to reconstruct the mode shapes directly from thermal data, enabling non-contact modal analysis of rotating structures.

Let K be the number of infrared images, where each image k captures out-of-plane vibrations of a structure undergoing in-plane rigid motion. The transformation matrix $\mathbf{Q}_k$, describing the rigid rotation between the k-th frame and the reference frame ($k = 0$), is estimated using corresponding corners of infrared-compatible ArUco markers detected in both the k-th and reference frames.

Let M be the number of detected markers. For each marker m ($m = 1, 2, \ldots, M$) and its c-th corner, let $\mathbf{P}_{m,c} = (i_{m,c}, j_{m,c}, 1)^T$ denote the homogeneous coordinates in the reference frame ($k = 0$), and $\mathbf{P'}_{m,c} = (i'_{m,c}, j'_{m,c}, 1)^T$ the corresponding coordinates in frame k. The transformation $\mathbf{Q}_k$ is computed to best align all $\mathbf{P'}_{m,c}$ with their counterparts $\mathbf{P}_{m,c}$. Fig. 1 illustrates the principle of this alignment, showing how the transformation $\mathbf{Q}_k$ and its inverse $\mathbf{Q}_k^{-1}$ are defined across frames.

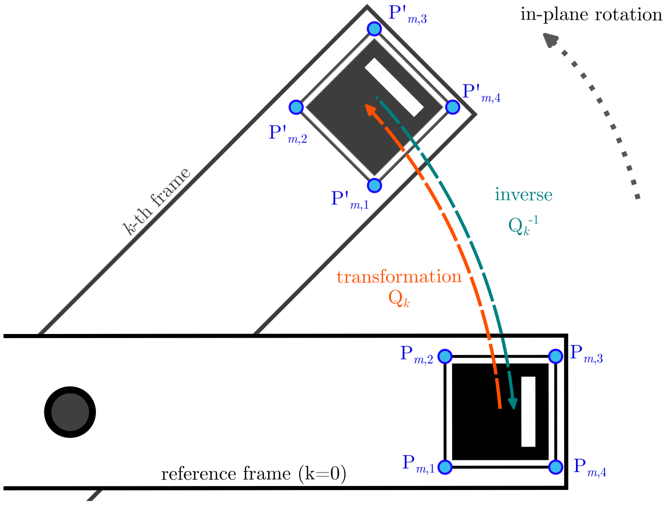

Figure 1: De-rotation using the inverse transformation $\mathbf{Q}_k^{-1}$, estimated from the corners of the m-th ArUco marker detected in both the k-th frame and the reference frame.

According to Eq. (11), once the transformation matrix $\mathbf{Q}_k$ is obtained, its inverse is applied to every point in frame k, effectively mapping the entire image content back to the coordinate system of the reference frame ($k = 0$):

$$\hat{\mathbf{P}} = \mathbf{Q}_k^{-1}\mathbf{P'}, \quad \forall \mathbf{P'} \in \text{frame } k. \tag{13}$$

Since the final thermoelasticity-based analysis focuses on the spatial distribution of temperature fluctuations, it is essential to preserve the spatial integrity of the de-rotated images during the transformation process. To ensure the de-rotation method accurately reflects the true spatial distribution, the quality of the transformation needs to be evaluated. This can be achieved by quantifying the alignment accuracy through the Euclidean error between the transformed marker corners coordinates and their reference positions. Such an evaluation helps validate the reliability of the estimated transformation matrices $\mathbf{Q}_k$, particularly in the presence of potential issues such as detection noise, marker occlusions, or interpolation artifacts introduced during the warping process. The overall transformation accuracy can be estimated by computing the mean value μ and standard deviation τ of the Euclidean error μ_k, which is calculated for each frame k across all M markers and their C coordinates. This error represents the deviation between the transformed marker corner coordinates $\hat{\mathbf{P}}_{m,c}$ and their reference positions in the initial frame ($k = 0$). To verify that the transformation precision is adequate, the de-rotation error should also be compared to the characteristic spatial scales of the analyzed phenomena. For instance, when extracting structural mode shapes, the typical mode wavelength should be much larger than the transformation error, ensuring that spatial patterns are not distorted by alignment inaccuracies.

The overall mean error μ and its standard deviation τ across frames are given by:

$$\mu = \frac{1}{K}\sum_k \mu_k, \quad \tau = \sqrt{\frac{1}{K}\sum_k (\mu_k - \mu)^2}. \tag{14}$$

The per-frame Euclidean error, μ_k, is defined as:

$$\mu_k = \frac{1}{MC}\sum_{m=1}^{M}\sum_{c=1}^{C} \left\|\mathbf{P}_{m,c} - \hat{\mathbf{P}}_{m,c}\right\|_2, \quad \forall k. \tag{15}$$

The standard deviation within each frame, denoted as τ_k, is given by:

$$\tau_k = \sqrt{\frac{1}{MC}\sum_{m=1}^{M}\sum_{c=1}^{C}\left(\left\|\mathbf{P}_{m,c} - \hat{\mathbf{P}}_{m,c}\right\|_2 - \mu_k\right)^2}. \tag{16}$$

After all K frames are realigned to the reference frame ($k = 0$) using $\mathbf{Q}_k^{-1}$ and Eq. (11), the stress variations $\Delta\sigma_{i,j}(t)$ at specific spatial locations are derived from the measured temperature signals, which are extracted from the motion-compensated video. The stress variation $\Delta\sigma$ at each pixel location (i, j), recorded at time t_k, is given by:

$$\Delta\sigma_{\hat{i},\hat{j}}(t_k) = \Delta\sigma_{i',j'}(t_k), \tag{17}$$

where (i', j') coordinates are reverted to $(\hat{i}, \hat{j})$ following Eq. (13). This allows the reconstruction of the time history of stress variations at each pixel in the reference frame:

$$\Delta\sigma_{i,j}(t) = \left\{\Delta\sigma_{i,j}(t_0), \Delta\sigma_{\hat{i},\hat{j}}(t_1), \ldots, \Delta\sigma_{\hat{i},\hat{j}}(t_{K-1})\right\}. \tag{18}$$

It is worth noting that the coordinates (i, j) of the first stress variation value in the reconstructed time history (Eq. (18)) are not marked with a hat symbol, since the first frame is used as the reference and no backward transformation is required for it.

Assuming the linear thermoelastic relationship between stress and temperature variation (Eq. (3)), the de-rotated stress-based time histories are obtained, and the full-field FRFs are estimated (Eq. (6)). Modal parameters are extracted from the FRFs using classical curve-fitting techniques, including LSCF and LSFD methods [54, 55]. Finally, mode shapes $\phi^{\sigma}_{i,j}$ are reconstructed from thermal measurements using the following expression [55]:

$$\phi^{\sigma}_{i,j} = \frac{A^{\Delta T}_{i,j}}{K_m\, \phi^{\sigma}_{i^*,j^*}}, \tag{19}$$

where $A^{\Delta T}_{i,j}$ represents the temperature response amplitude at pixel (i, j), and $\phi^{\sigma}_{i^*,j^*}$ is the stress mode shape at a selected normalization point. The coefficient K_m accounts for the proportionality between temperature and stress, as derived from the thermoelastic relationship (Eq. (18)).

4. Experimental research

This section provides a description of the setup developed for the roto-vibration experiments, outlines the infrared measurement protocol, and discusses the data processing methodology.

4.1. Experimental setup

An aluminum beam, with dimensions 500×30×2.5 mm, was mounted on a shaft and inserted into a clamping sleeve bearing. The assembly was then installed on an electrodynamical shaker (Sentek L1024M), enabling out-of-plane vibrations and allowing in-plane free rotation of the beam around its center point (see Fig. 2).

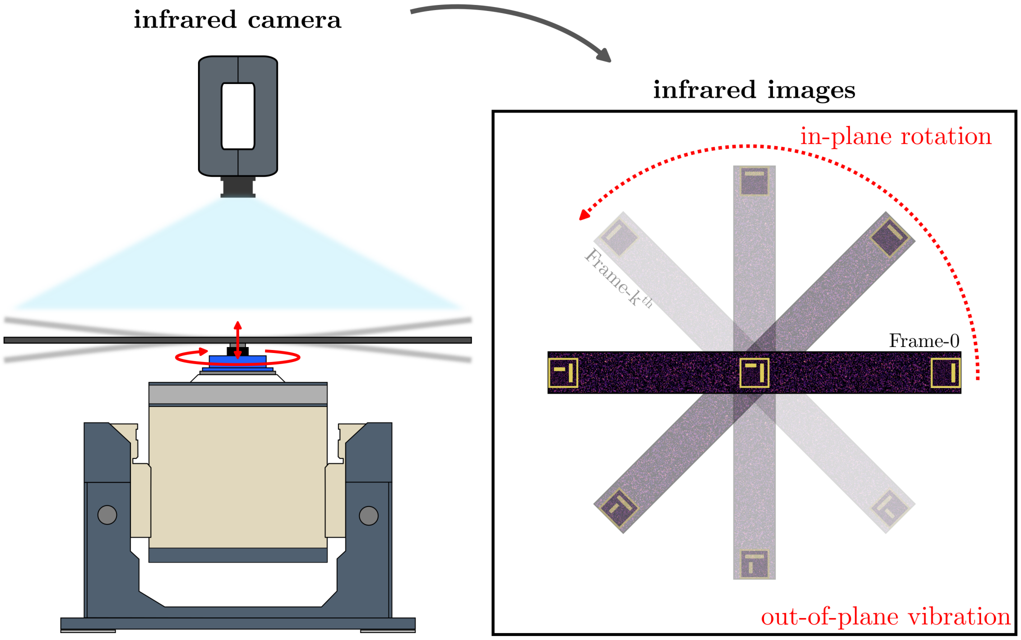

Figure 2: Schematic of experimental setup and infrared images collected.

To enhance the thermoelastic effect and minimize infrared reflection from the surroundings, the top surface of the beam was coated with high-emissivity black paint (Black Wrapper Spray, 4R) [29]. Additionally, 20×20 mm Original-Dictionary ArUco markers were placed on the top surface to facilitate rigid-body motion tracking and compensation [41]. The markers were manufactured in-house using laser-cut black-matte vinyl layer adhered to a high-reflectivity tape, enhancing contrast and improving marker detection in the infrared spectrum. In this study, three ArUco markers from the Original-Dictionary were used [41]: two positioned at each end of the beam, and one placed on top of the center of rotation (i.e., the shaker's vertical axis). While additional markers could provide more corner points and enable overdetermined transformations with iterative refinement (e.g., nonlinear least squares), the chosen configuration balances geometric robustness with the need to leave most of the structure's surface unobstructed for subsequent infrared-based analysis.

For research purposes, preliminary measurements were conducted under vibration-only conditions using a control accelerometer (PCB 352C23/NC) installed on the shaker plate, and a response accelerometer (PCB 352C23), installed on the top-surface of the beam, acquiring at 25600 Hz. These measurements identified two natural frequencies below 200 Hz (27.3 Hz and 173.4 Hz). Similarly to the experimental approach adopted by Zaletelj et al. [35], in this study the excitation amplitude was determined by gradually increasing it to evaluate the sensitivity of the infrared camera response and to identify the minimum detectable surface stress. Based on these findings, the final experiments employed a pseudo-random excitation signal within the 15–200 Hz range (RMS = 13.6 g), generated by a Siemens LMS SCADAS and amplified by a Sentek PA115 amplifier.

4.2. Infrared measurements

An infrared camera (FLIR A6751sc, equipped with a 25 mm lens) was used to measure surface temperature variations on the beam. The camera captures up to 400 frames per second at a resolution of 320×256 pixels, with a Noise Equivalent Temperature Difference (NETD) of 18 mK and a 14-bit depth resolution. The combination of frame rate, resolution, and calibrated radiometric settings led to an integration time of 0.9781 μs, which effectively suppressed motion blur while maintaining sufficient infrared signal quality. The infrared imaging and acceleration data were acquired for 10 seconds, resulting in a frequency resolution of 1/10 Hz, ensuring the same resolution in the frequency-domain regardless of differences in sampling frequency. As shown in Fig. 3, the infrared camera was positioned above the shaker, using a vibration-isolated tripod, at a sensor-to-target distance of 1.5 meters, capturing approximately one quarter of the full in-plane rotation.

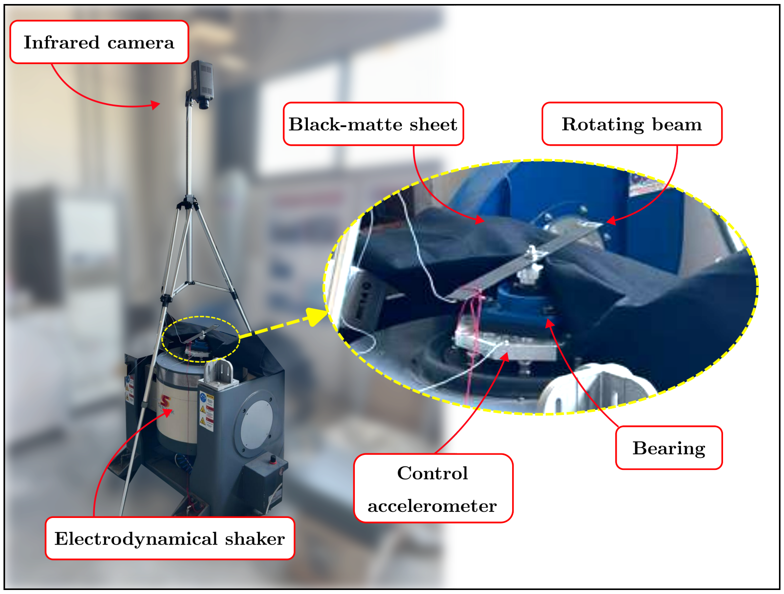

Figure 3: Experimental setup: infrared camera, control accelerometer, and rotating beam installed on the electrodynamical shaker.

Prior to the infrared-vibration measurements, the camera's perpendicular alignment to the rotational plane was verified by leveraging the detected corners of the same ArUco markers later used in the analysis. The markers were expected to appear as a square with no tilt: any visible perspective distortion, indicating misalignment, was adjusted accordingly. Due to symmetry considerations and field-of-view limitations under the specified acquisition conditions, only half-beam rotation was recorded. In this configuration, two infrared markers were visible in the scene: one positioned at the beam's end (ID-0) and the other at the center of rotation (ID-1), ensuring that relevant stress distributions remained unobstructed. The thermoelastic coefficient $K_m = 2.53 \times 10^{-9}$ [°C/Pa] was obtained by averaging 10 measurements under harmonic loading (20–110 Hz), correlating IR-measured surface temperature fluctuations with local stress derived from strain gauge data via Lamé's equation [35]. The strain gauge (HBM 1-LY13-6/350) was placed in a high-signal-to-noise ratio, low-gradient region [32].

To assess the impact of operating conditions on ArUco-based transformation accuracy, tests were conducted by varying the rotational speed and camera sampling rate. The frames-per-degree metric η quantifies inter-frame motion and enables consistent comparison across different operating scenarios. It is defined as the ratio of the sampling rate f_s (in Hz) to the rotational speed ω (in rpm), expressed as:

$$\eta = \frac{f_s}{\omega \times 360/60} = \frac{f_s}{6\,\omega} \quad \text{[frames/degree]}, \tag{20}$$

where the factor $360/60 = 6$ converts ω from rpm to degrees per second.

A representative test case (0.9 rpm, 400 Hz) was selected for further analysis, as it provided the largest observed rotation angle (54°) over the 10-second measurement time while maintaining full visibility of the structure within the camera's field of view. Additional tests were performed to evaluate alignment performance across a broader range of motion conditions, represented by η values spanning from 17 to 100 frames-per-degree. These were achieved by varying the rotational speed while maintaining a fixed sampling frequency of 400 Hz. Specifically, tests were conducted at $\eta = 100$, 74, 51, and 17, corresponding to rotational speeds of approximately 0.67, 0.9, 1.3, and 3.92 rpm, respectively. Although broader operating conditions are in principle supported by the methodology, the selected values reflect a practical balance between coverage and the constraints of the available acquisition setup.

4.3. Infrared images processing

Each infrared video was initially processed to detect ArUco markers and extract their corner coordinates in each frame. To ensure accurate marker detection fin the infrared images, pre-processing steps were applied when needed, including adaptive histogram equalization for contrast enhancement, Gaussian blurring to suppress high-frequency noise, and adaptive thresholding to highlight edge features [58]. These operations were used exclusively to support marker detection and transformation estimation. In fact, to preserve the fidelity of pixel intensities required for subsequent thermoelasticity-based analysis, all further processing and evaluation were performed directly on the raw, de-rotated infrared data. Marker detection was performed independently in each frame using the unique IDs of the ArUco markers [58]. This frame-by-frame detection improves robustness to temporary occlusion and enables reliable matching even under significant motion between frames. After detection, the marker corners were used to compute the geometric transformation between each frame and a reference. To improve the accuracy of the estimated transformation, OpenCV's built-in RANSAC-based estimators were used to compute the mapping between marker corners [58].

These functions apply the RANSAC algorithm to iteratively exclude outlier correspondences, enhancing robustness to detection noise and spurious corner readings [59]. It is important to recognize that out-of-plane vibrations cause vertical displacements, which can shift the apparent position of surface points on the pixel grid and potentially affect the recorded pixel intensities used in thermoelastic analysis. Although these effects are inherent to vertical excitation, they were not explicitly quantified in this study. Nonetheless, the experimental setup was designed to promote predominantly planar motion and minimize significant vertical displacements.

According to the proposed methodology, the Euclidean transformation matrices $\mathbf{Q}_k$ were computed, and, following Eq. (12), their inverse $\mathbf{Q}_k^{-1}$ were then applied to their corresponding frames, aligning them back to the coordinate system of frame $k = 0$. The accuracy of this reverting process was quantified using Eq. (15) and Eq. (16).

Following spatial alignment, the stress time series were built, as per Eq. (18), and transformed into the frequency domain, where FRFs were estimated using Welch's method with a 50% Hann window function, which reduces spectral leakage within each analysis segment and improves the stability of frequency-domain estimates. From the resulting spectral data, modal parameters were identified, and the full-field mode shapes were obtained using Eq. (19).

5. Results and discussion

The pre-processing of the acquired infrared images enabled reliable detection of the infrared-compatible ArUco markers throughout the measurement sequence. Fig. 4 illustrates the first, intermediate, and last infrared frames, where the detected markers are clearly visible.

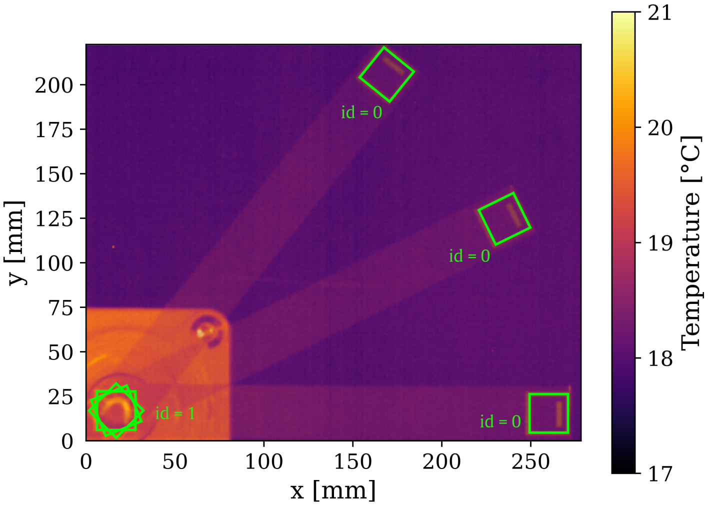

Figure 4: Averaged first, intermediate, and last infrared images with detected ArUco markers.

The tracked marker corner coordinates $\mathbf{P}_{m,c}$ and $\mathbf{P'}_{m,c}$ across the acquisition period are shown in Fig. 5.

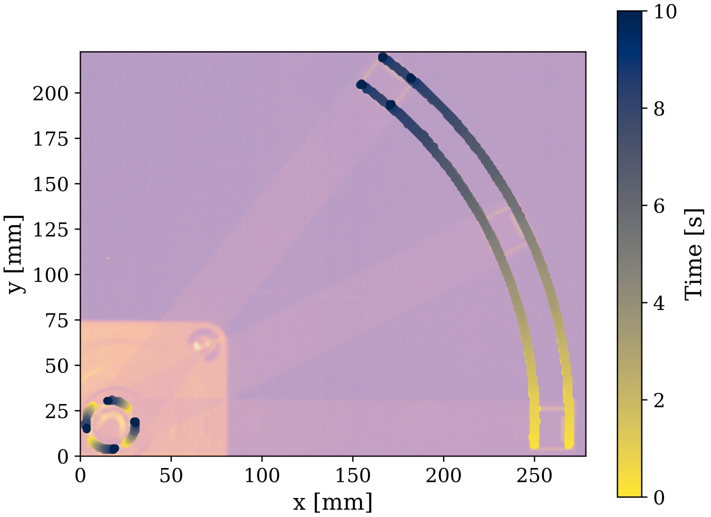

Figure 5: Time evolution of ArUco marker corners $\mathbf{P'}_{m,c}$, overlaid on blended first, intermediate, and last infrared images.

As expected, the bottom-left corner of the marker placed at the center of rotation traces a circular trajectory. In contrast, the corners of the marker located at the beam's free end follow a wider arc, consistent with a total angular displacement of approximately 54° (0.9 rpm over 10 seconds).

As detailed in Sec. 3, in case of pure rigid-body rotation, a single matching marker ID per frame pair (from frame-0 to frame-k) is sufficient to accurately determine the Euclidean transformation, as the four corners of the marker provide enough geometric constraints. For more complex transformations involving deformation or marker occlusion, incorporating multiple marker IDs per frame significantly improves transformation robustness.

Using the detected corner coordinates, the transformation matrices $\mathbf{Q}_k$ were computed and subsequently inverted to compensate for rotation and realign each frame to the initial configuration. The resulting back-projected marker coordinates $\hat{\mathbf{P}}_{m,c}$, and the warped infrared frames, are presented in Fig. 6.

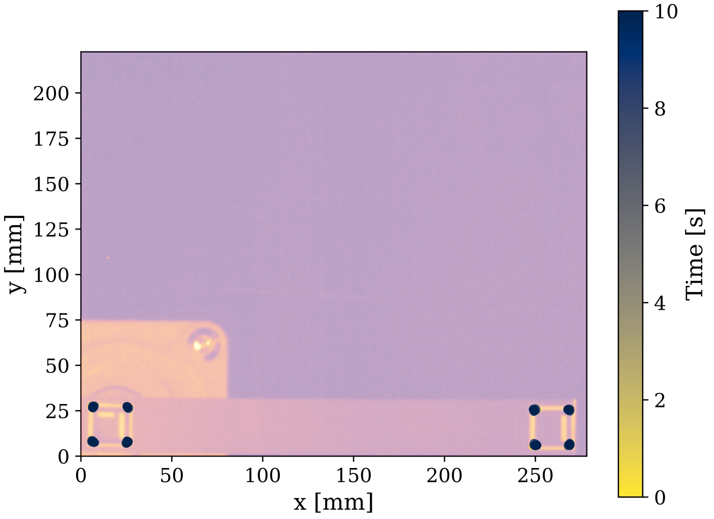

Figure 6: Time evolution of ArUco marker corner coordinates after applying inverse transformations $\mathbf{Q}_k^{-1}$ to compensate for rotation.

The overall transformation accuracy was quantified by computing the mean Euclidean error per frame, μ_k, and the global transformation error μ, along with their standard deviations, τ_k and τ, respectively. These values reflect the average discrepancy between the original and back-projected marker coordinates with respect to the frame-0 reference system.

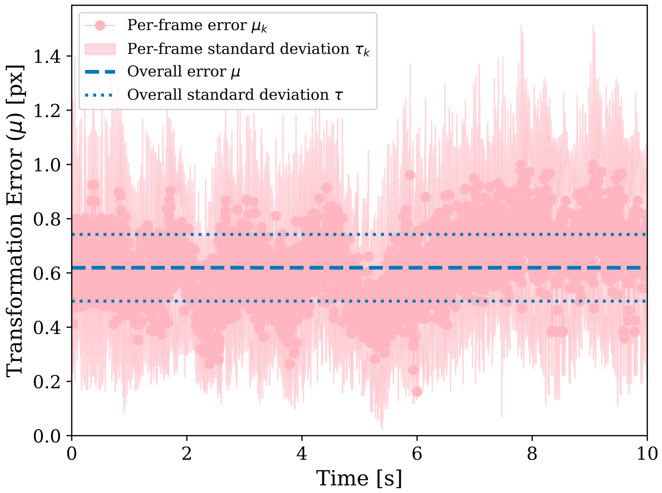

Figure 7: Per-frame transformation errors μ_k and overall transformation error μ (with standard deviations), obtained by back-projecting marker coordinates to the frame-0 reference system.

Sub-pixel transformation errors were achieved, indicating excellent performance of the proposed alignment technique. Nevertheless, it is worth emphasizing that in thermoelasticity-based measurements, the primary focus is on spatial distributions of surface temperature variations rather than precise point-wise alignment, as is common in kinematic-based optical methods. Therefore, even when transformation errors μ exceed the pixel level (super-pixel errors), the alignment may still be adequate for reliable extraction of mode shapes and other global phenomena, as long as the overall spatial distribution is preserved. Further investigation is needed to establish acceptable thresholds for transformation errors, beyond which the fidelity of thermoelastic signal interpretation may be compromised. Such thresholds may vary depending on the spatial resolution, thermal sensitivity, and application-specific constraints.

The influence of the frames-per-degree ratio, denoted as η, on the transformation accuracy is shown in Fig. 8. This parameter captures the number of frames acquired per degree of rotation.

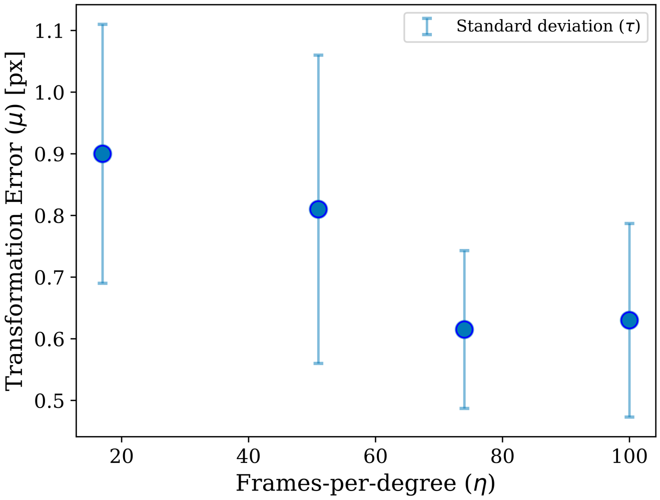

Figure 8: Effect of the frames-per-degree ratio η on transformation error μ based on ArUco marker detection.

As expected, higher values of η, corresponding to slower motion or higher frame rates, result in reduced inter-frame angular displacement, thereby lowering the transformation error. This is because smaller apparent motion leads to more accurate marker detection and reduced geometric distortion. Conversely, when η is low (i.e., larger inter-frame motion), the algorithm becomes more sensitive to noise, motion blur, and environmental variability, which can degrade the transformation accuracy. These results highlight the importance of inter-frame motion in determining transformation accuracy and support the use of η as a practical metric for comparing different acquisition scenarios. By condensing the combined effect of frame rate and rotational speed into a single parameter, η enables consistent and scalable evaluation of alignment performance across a range of test conditions.

Finally, classical experimental modal analysis techniques were employed to compute the FRF of the structure from control accelerometer and thermal/stress response measurements, enabling the identification of its dynamic characteristics. Full-field mode shapes were successfully extracted from the processed infrared image sequence. To attenuate spatial noise and enhance the clarity of the mode shape distributions, a mild 5×5 pixel Gaussian filter was applied to the temperature field. Fig. 9 shows an infrared snapshot, highlighting the region of interest where the FRF and mode shapes were computed, along with the extracted mode shapes and the corresponding FRF spectrum.

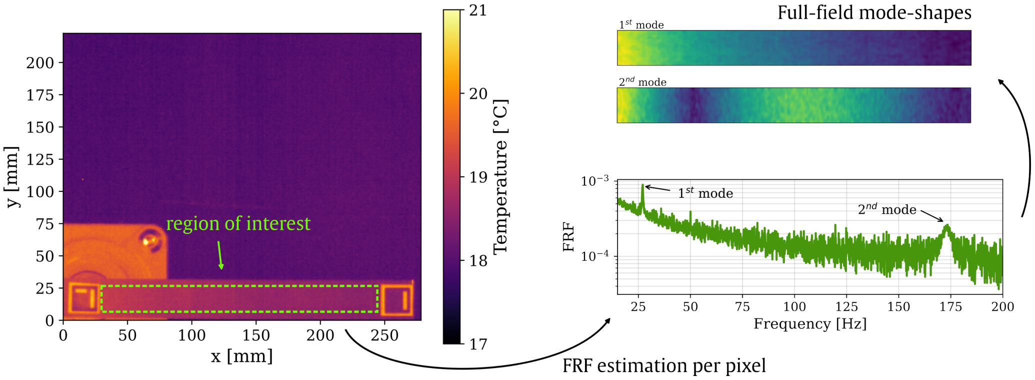

Figure 9: Annotated de-rotated infrared image of the experimental setup showing the defined region of interest (left). Extracted full-field mode shapes corresponding to the first (top) and second (middle) natural frequencies, and the Frequency Response Function (FRF) used to identify modal frequencies (bottom).

Two natural frequencies were identified at 27.3 Hz and 173.4 Hz, which are in good agreement with reference measurements, preliminary performed in the vibration-only condition. The corresponding mode shapes exhibit spatial distributions consistent with theoretical expectations.

6. Conclusion

Rotating structures present a challenge to traditional contact-based measurement techniques, especially under vibrational excitation. Optical methods like infrared thermography offer a non-contact alternative, but are typically limited to capturing static or slowly varying temperature fields. In contrast, thermoelasticity exploits high-speed thermal imaging to detect stress-induced temperature fluctuations, enabling the analysis of structural vibrations in rotating components.

This work demonstrates that combining thermoelastic imaging with computer-vision techniques provides a robust, full-field approach to the non-contact monitoring of rotating structures. Infrared-compatible ArUco markers were used to track and compensate for rigid body rotation, allowing for the isolation of dynamic thermal responses associated with structural vibrations. While the current implementation focused on rigid rotations, the methodology is extendable to more complex motions, including roto-translations and general affine transformations. Experimental modal analysis confirmed the ability to extract full-field mode shapes from the compensated thermoelastic data. An uncertainty analysis demonstrated sub-pixel accuracy of the transformation process across varying operating conditions. In addition, the frames-per-angle ratio was introduced as a metric to evaluate the influence of operating and measurement scenarios on the transformation accuracy.

The integration of computer-vision and thermoelasticity offers a significant advancement for structural health monitoring of rotating systems. This approach enables accurate motion compensation and opens new perspectives for real-time, non-contact diagnostics and damage detection in dynamically loaded components.

Acknowledgments

The authors acknowledge financial support from the European Union under the Horizon-WIDERA-2023-TALENTS-02-01 topic, through the Marie Skłodowska-Curie grant agreement No. 101180595, and from the Slovenian Research Agency (research core funding No. P2-0263).

Declaration of Competing Interest

The authors declare that they have no known competing financial interests or personal relationships that could have appeared to influence the work reported in this paper.

References

[1] D. Benasciutti, Fatigue analysis of random loadings, Ph.D. thesis, University of Ferrara, Italy (2004).

[2] Z. L. Mahri, M. S. Rouabah, Fatigue Estimation for a Rotating Blade of a Wind Turbine, Journal of Renewable Energies 5 (1) (2002) 39–47. `doi:10.54966/JREEN.V5I1.885`.

[3] D. J. Ewins, Modal testing: theory, practice and application, 2nd Edition, Wiley, 2009.

[4] A. Ghoshal, M. J. Sundaresan, M. J. Schulz, P. Frank Pai, Structural health monitoring techniques for wind turbine blades, Journal of Wind

Engineering and Industrial Aerodynamics 85 (3) (2000) 309–324. doi:10.1016/S0167-6105(99)00132-4.

[5] Q. Leclère, H. André, J. Antoni, A. Burel, C. Capdessus, M. Cocconcelli, G. D'Elia, A. P. Daga, J. L. Dion, M. El Badaoui, A. El Hidali, L. Garibaldi, F. Girardin, J. Griffaton, K. Gryllias, Y. Han, J. Helsen, F. Karkafi, K. Kestel, L. Kordylas, D. Kunte, S. Lo Feudo, A. Marsick, D. Marx, A. R. Mauricio, J. Miranda-Fuentes, C. Peeters, T. Poupon, D. Rémond, F. Renaud, J. Roussel, J. Touzet, T. Verwimp, L. Viale, M. Yazdanianasr, R. Zhu, Video-based diagnosis of a rolling element bearing using a high-speed camera: Feedback on the Survishno 2023 conference contest, Mechanical Systems and Signal Processing 230 (2025) 112601. doi:10.1016/J.YMSSP.2025.112601.

[6] P. Russhard, The Rise and Fall of the Rotor Blade Strain Gauge, Mechanisms and Machine Science 23 (2015) 27–37. doi:10.1007/978-3-319-09918-7{_}2.

[7] G. Allevi, L. Capponi, P. Castellini, P. Chiariotti, F. Docchio, F. Freni, R. Marsili, M. Martarelli, R. Montanini, S. Pasinetti, A. Quattrocchi, R. Rossetti, G. Rossi, G. Sansoni, E. P. Tomasini, Investigating Additive Manufactured Lattice Structures: A Multi-Instrument Approach, Transactions on Instrumentation and Measurement 69 (5) (2020) 2459–2467. doi:10.1109/TIM.2019.2959293.

[8] Y. Kato, S. Watahiki, Vibration mode identification method for structures using image correlation and compressed sensing, Mechanical Systems and Signal Processing 199 (2023) 110495. doi:10.1016/J.YMSSP.2023.110495.

[9] P. J. Schubel, R. J. Crossley, E. K. Boateng, J. R. Hutchinson, Review of structural health and cure monitoring techniques for large wind turbine blades, Renewable Energy 51 (2013) 113 – 123. doi:10.1016/j.renene.2012.08.072.

[10] J. Baqersad, P. Poozesh, C. Niezrecki, P. Avitabile, Photogrammetry and optical methods in structural dynamics – A review, Mechanical Systems and Signal Processing 86 (2017) 17 – 34. doi:10.1016/j.ymssp.2016.02.011.

[11] J. Javh, J. Slavič, M. Boltežar, The subpixel resolution of optical-flow-based modal analysis, Mechanical Systems and Signal Processing 88 (2017) 89–99. doi:10.1016/j.ymssp.2016.11.009.

[12] I. Tomac, J. Slavič, D. Gorjup, Single-pixel optical-flow-based experimental modal analysis, Mechanical Systems and Signal Processing 202 (2023). doi:10.1016/j.ymssp.2023.110686.

[13] Y. Hu, S. Li, Y. Xia, Y. Yang, A super-sensitivity incoherent optical method with time-delay embedding for pixel-limited dynamic displacement measurements, Mechanical Systems and Signal Processing 230 (2025) 112546. doi:10.1016/J.YMSSP.2025.112546.

[14] Z. Luo, B. Merainani, V. Baltazart, Q. Zhang, M. Döhler, Subpixel motion estimation for video-based target-free vibration monitoring under complex environmental conditions, Mechanical Systems and Signal Processing 226 (2025) 112342. doi:10.1016/J.YMSSP.2025.112342.

[15] R. Huňady, P. Pavelka, P. Lengvarský, Vibration and modal analysis of a rotating disc using high-speed 3D digital image correlation, Mechanical Systems and Signal Processing 121 (2019) 201–214. doi:10.1016/J.YMSSP.2018.11.024.

[16] J. Huang, K. Zhou, W. Chen, H. Song, A pre-processing method for digital image correlation on rotating structures, Mechanical Systems and Signal Processing 152 (2021) 107494. doi:10.1016/J.YMSSP.2020.107494.

[17] Y. Chen, D. T. Griffith, Experimental and numerical full-field displacement and strain characterization of wind turbine blade using a 3D Scanning Laser Doppler Vibrometer, Optics and Laser Technology 158 (2023) 108869. doi:10.1016/j.optlastec.2022.108869.

[18] B. Gwashavanhu, A. J. Oberholster, P. S. Heyns, Rotating blade vibration analysis using photogrammetry and tracking laser Doppler vibrometry, Mechanical Systems and Signal Processing 76-77 (2016) 174–186. doi:10.1016/J.YMSSP.2016.02.019.

[19] Y. Y. Hung, Shearography: A New Optical Method For Strain Measurement And Nondestructive Testing, https://doi.org/10.1117/12.7972920 21 (3) (1982) 391–395. doi:10.1117/12.7972920.

[20] S. Hwang, Y. K. An, H. Sohn, Continuous Line Laser Thermography for Damage Imaging of Rotating Wind Turbine Blades, Procedia Engineering 188 (2017) 225–232. doi:10.1016/J.PROENG.2017.04.478.

[21] B. F. Knisely, R. A. Berdanier, K. A. Thole, C. W. Haldeman, J. R. Markham, J. E. Cosgrove, A. E. Carlson, J. J. Scire, Acquisition and processing considerations for infrared images of rotating turbine blades, Journal of Turbomachinery 143 (4) (4 2021). doi:10.1115/1.4050143/1098228.

[22] G. Zhou, Z. C. Ong, Z. Zhang, W. Yin, H. Chen, H. Ma, Y. Fu, Defect detection of carbon fiber deflectors based on laser infrared thermography and experimental modal analysis, Mechanical Systems and Signal Processing 221 (2024) 111763. doi:10.1016/J.YMSSP.2024.111763.

[23] M. Sisti, C. Falsetti, P. F. Beard, Infrared temperature measurements on fast moving targets: A novel calibration approach, Measurement 225 (2024) 113870. doi:10.1016/J.MEASUREMENT.2023.113870.

[24] G. Pitarresi, Lock-In Signal Post-Processing Techniques in Infra-Red Thermography for Materials Structural Evaluation, Experimental Mechanics 55 (4) (2015) 667–680. doi:10.1007/S11340-013-9827-1/FIGURES/12.

[25] W. Weber, Ueber die specifische Wärme fester Körper, insbesondere der Metalle, Annalen der Physik 96 (10) (1830) 177 – 213. doi:10.1002/andp.18300961002.

[26] W. Thomson, XV. On the Dynamical Theory of Heat, with numerical results deduced from Mr Joule's Equivalent of a Thermal Unit, and M. Regnault's Observations on Steam, Transactions of the Royal Society of Edinburgh 20 (2) (1853) 261 – 288. doi:10.1017/S0080456800033172.

[27] K. T. Compton, D. B. Webster, Temperature changes accompanying the adiabatic compression of steel, Physical Review 5 (2) (1915) 159 – 166. doi:10.1103/PhysRev.5.159.

[28] G. Pitarresi, E. A. Patterson, A review of the general theory of thermoelastic stress analysis, Journal of Strain Analysis for Engineering Design 38 (5) (2003) 405 – 417. doi:10.1243/03093240360713469.

[29] W. N. Sharpe, Springer handbook of experimental solid mechanics (2008).

[30] C. Braccesi, F. Cianetti, M. Moretti, G. Rossi, Random Loads Fatigue. Experimental Approach through Thermoelasticity, Procedia Engineering 101 (C) (2015) 312–321. `doi:10.1016/J.PROENG.2015.02.038`.

[31] Z. Stankovičová, V. Dekýš, P. Novák, B. Strnadel, Detection of Natural Frequencies Using IR Camera, Procedia Engineering 192 (2017) 830–833.

[32] L. Capponi, J. Slavič, G. Rossi, M. Boltežar, Thermoelasticity-based modal damage identification, International Journal of Fatigue 137 (2020) 105661. `doi:10.1016/j.ijfatigue.2020.105661`.

[33] J. Molina-Viedma, L. Felipe-Sesé, E. López-Alba, F. A. Díaz, Thermoelastic effect in modal shapes at high frequencies using infrared thermography, Measurement 176 (2021) 109180. `doi:10.1016/J.MEASUREMENT.2021.109180`.

[34] A. J. Molina-Viedma, L. Felipe-Sesé, E. López-Alba, F. A. Díaz, Comparison of lock-in correlation and a novel periodogram method for experimental multi-harmonic thermoelastic analysis, Mechanical Systems and Signal Processing 164 (2 2022). `doi:10.1016/j.ymssp.2021.108235`.

[35] K. Zaletelj, J. Slavič, J. Šonc, M. Boltežar, Strain experimental modal analysis of an Euler–Bernoulli beam based on the thermoelastic principle, Mechanical Systems and Signal Processing 201 (2023) 110655. `doi:10.1016/J.YMSSP.2023.110655`.

[36] J. Šonc, K. Zaletelj, J. Slavič, Application of thermoelasticity in the frequency-domain multiaxial vibration-fatigue criterion, Mechanical Systems and Signal Processing 224 (2025) 112002. `doi:10.1016/J.YMSSP.2024.112002`.

[37] T. Sakagami, N. Yamaguchi, S. Kubo, T. Nishimura, A new full-field motion compensation technique for infrared stress measurement using digital image correlation, The Journal of Strain Analysis for Engineering Design 43 (6) (2008) 539–549. `doi:10.1243/03093247JSA360`.

[38] M. L. Silva, G. Ravichandran, Combined thermoelastic stress analysis and digital image correlation with a single infrared camera, Journal of Strain Analysis for Engineering Design 46 (8) (2011) 783–793. doi:10.1177/0309324711418286.

[39] T. Tocci, L. Capponi, R. Marsili, G. Rossi, Optical-flow-based motion compensation algorithm in thermoelastic stress analysis using single-infrared video, Acta IMEKO 10 (4) (2021) 169–176. doi:10.21014/acta{_}imeko.v10i4.1147.

[40] G. Tribbiani, T. Zara, T. Truffarelli, L. Capponi, Fiducial marker and blob detection-based motion compensation algorithm for Thermoelastic Stress Analysis measurements, Journal of Physics: Conference Series 2698 (1) (2024) 012001. doi:10.1088/1742-6596/2698/1/012001.

[41] S. Garrido-Jurado, R. Muñoz-Salinas, F. J. Madrid-Cuevas, M. J. Marín-Jiménez, Automatic generation and detection of highly reliable fiducial markers under occlusion, Pattern Recognition 47 (6) (2014) 2280–2292. doi:10.1016/J.PATCOG.2014.01.005.

[42] F. J. Romero-Ramirez, R. Muñoz-Salinas, R. Medina-Carnicer, Speeded up detection of squared fiducial markers, Image and Vision Computing 76 (2018) 38–47. doi:10.1016/J.IMAVIS.2018.05.004.

[43] T. Tocci, L. Capponi, G. Rossi, ArUco marker-based displacement measurement technique: uncertainty analysis, Engineering Research Express 3 (3) (2021) 035032. doi:10.1088/2631-8695/AC1FC7.

[44] G. Čepon, D. Ocepek, M. Kodrič, M. Demšar, T. Bregar, M. Boltežar, Impact-Pose Estimation Using ArUco Markers in Structural Dynamics, Experimental Techniques 48 (2) (2024) 369–380. doi:10.1007/S40799-023-00646-0/FIGURES/17.

[45] R. M. Claro, D. B. Silva, A. M. Pinto, ArTuga: A novel multimodal fiducial marker for aerial robotics, Robotics and Autonomous Systems 163 (2023) 104398. doi:10.1016/J.ROBOT.2023.104398.

[46] R. T. Potter, L. J. Greaves, The application of thermoelastic stress analysis techniques to fibre composites, Optical Engineering 817 (1987) 134 – 146. doi:10.1117/12.967419.

[47] A. K. Wong, J. G. Sparrow, S. A. Dunn, On the revised theory of the thermoelastic effect, Journal of Physics and Chemistry of Solids 49 (4) (1988) 395 – 400. doi:10.1016/0022-3697(88)90099-6.

[48] J. M. Dulieu-Smith, Alternative calibration techniques for quantitative thermoelastic stress analysis, Strain 31 (1) (1995) 9 – 16. doi:10.1111/j.1475-1305.1995.tb00949.x.

[49] M. H. Belgen, Infrared radiometric stress instrumentation application range study, Tech. rep., National Aeronautics and Space Administration (1968).

[50] J. M. Dulieu-Barton, P. Stanley, Development and applications of thermoelastic stress analysis, Journal of Strain Analysis for Engineering Design 33 (2) (1998) 93 – 104. doi:10.1243/0309324981512841.

[51] N. Harwood, W. M. Cummings, Calibration of the thermoelastic stress analysis technique under sinusoidal and random loading conditions, Strain 25 (3) (1989) 101 – 108. doi:10.1111/j.1475-1305.1989.tb00701.x.

[52] N. M. M. Maia, J. M. M. Silva, Modal analysis identification techniques, Philosophical Transactions of the Royal Society of London. Series A: Mathematical, Physical and Engineering Sciences 359 (1778) (2001) 29–40. doi:10.1098/rsta.2000.0712.

[53] J. Slavič, M. Boltezar, M. Mrsnik, M. Cesnik, J. Javh, Vibration Fatigue by Spectral Methods: From Structural Dynamics to Fatigue Damage–Theory and Experiments, Elsevier, 2020. doi:https://doi.org/10.1016/C2019-0-04580-3.

[54] P. Guillaume, L. Hermans, H. Van Der Auweraer, Maximum likelihood identification of modal parameters from operational data, in: Proceedings of SPIE - The International Society for Optical Engineering, 1999.

[55] B. Cauberghe, Applied frequency-domain system identification in the field of experimental and operational modal analysis (2004).

[56] R. Hartley, A. Zisserman, Multiple View Geometry in Computer Vision, 2004.

[57] R. C. Gonzalez, R. E. Woods, Digital Image Processing, 2018.

[58] G. Bradski, A. Kaehler, Learning OpenCV: Computer vision with the OpenCV library, 2008.

[59] M. A. Fischler, R. C. Bolles, Random sample consensus: A Paradigm for Model Fitting with Applications to Image Analysis and Automated Cartography, Communications of the ACM 24 (6) (1981) 381–395. `doi:10.1145/358669.358692`.